Snapshot Partially Coherent Diffraction Tomography

Bo Xiong,[1,2,‡] Xiaoxu Li,[1,2,‡] You Zhou,[3] Liejun Wang,[4] Jiamin Wu,[1,2,*] and Qionghai Dai[1,2,†]

[1] *Department of Automation, Tsinghua University, Beijing, 100084, China*

[2] *Beijing Key Laboratory of Multi-dimension & Multi-scale Computational Photography (MMCP), Tsinghua University, Beijing 100084, China*

[3] *School of Electronic Science and Engineering, Nanjing University, Nanjing 210023, China*

[4] *School of Information Science and Engineering, Xinjiang University, Urumqi 830046, China*

(Received 3 January 2021; accepted 1 April 2021; published 28 April 2021)

Diffraction tomography is a promising label-free three-dimensional (3D) imaging method for transparent samples due to its low phototoxicity. However, it usually requires coherent illuminations and massive measurements, which will, respectively, introduce speckle noises and time-consuming acquisitions, and thus, limit its applications in multicellular dynamic organisms. To address these problems, here we propose a partially coherent and snapshot diffraction tomography method based on light-field microscopy. By incorporating the illumination optical transfer function into the volumetric differential phase contrast model, we obtain a 3D phase stack from the snapshot four-dimensional phase-space measurements. Then a 3D phase-point-spread function is used for 3D deconvolution to achieve computational optical sectioning and enhance the resolution, and finally, we extract 3D refractive-index information from the 3D phase stack. Experiments on freely moving *Caenorhabditis elegans* are shown accordingly, demonstrating the great potential of the proposed method for label-free 3D imaging of multicellular organisms *in vivo* at high speed up to the camera frame rate.

DOI: 10.1103/PhysRevApplied.15.044048

I. INTRODUCTION

Observing three-dimensional (3D) organisms in their native state without labeling has long been a pursuit in biology [1–3]. However, the transparent property of cells leads to extremely low contrast in absorption, posing great challenges in intensity-based imaging. Fortunately, the nonuniform 3D distributions of the refractive index (RI) have strong contrasts in phase information, which can be converted into intensity by phase-contrast microscopy [4,5]. In the last decade, quantitative phase imaging (QPI) has attracted great attention in various fields because it provides an accurate quantification of local phase shifts [6,7] and exhibits substantially less phototoxicity than fluorescence imaging [1,8]. More importantly, since the phase information can be represented as an integral of the RI along a specific light path, the 3D RI map can be retrieved through multiple quantitative phase measurements of different illumination angles [2,9] or different focal planes [1].

There are mainly two types of QPI methods: coherent and partially coherent illuminations [7]. Digital holography is a typical example of coherent QPI with strong contrast induced by the interference from a coherent light source. Usually, the speed of coherent QPI for 3D RI tomography is limited; however, the combination of a digital micromirror device and a graphic processing unit (GPU) enables video-rate imaging and visualization [10]. Good phase sensitivity of coherent QPI provides both high resolution and a high signal-to-noise ratio for thin samples, such as cultured cells, but it is disadvantageous for thick samples with scattering due to speckle effects [11–13]. To eliminate speckles, many techniques are proposed with partially coherent illuminations, such as differential-phase-contrast (DPC) imaging [14], the transport-of-intensity equation [15], intensity diffraction tomography [16], and quantitative oblique back-illumination microscopy [17]. To further improve the imaging speed, various works have been exploited recently to achieve snapshot QPI through some modifications to both hardware [18,19] and software [20,21]. However, extending the limited depth of field (DOF) of partially coherent QPI within a snapshot has barely been investigated. Since partially coherent illumination has a short coherence length in both spatial and temporal domains, the DOF is smaller than that of coherent QPI. It is good for the optical sectioning requirement of phase tomography, but it is unfavorable for dynamic samples with a large volume. Besides, multiple measurements

*wujiamin@tsinghua.edu.cn

†daiqionghai@mail.tsinghua.edu.cn

‡These authors contributed equally to this work.

are always required to achieve a volumetric QPI or 3D RI map with partially coherent illumination, in either the axial domain [1,22,23] or the angular domain [24–26]. The time-consuming sequential acquisition of multiple measurements greatly limits its application for *in vivo* imaging. Even with multiplexed illumination strategies and sparse-prior-based reconstruction [26,27], dense measurements are still required for large-volume 3D QPI at the current stage. In addition to the loss of temporal resolution, the motion of living organisms will introduce strong artifacts into the 3D reconstruction.

To address these problems, we propose a snapshot partially coherent diffraction tomography method by harnessing the unique capabilities of light-field microscopy (LFM). With a microlens array inserted at the image plane of a normal bright-field microscope, LFM captures the four-dimensional (4D) phase-space measurements within a snapshot. However, traditional LFM is usually focused on two-dimensional phase imaging [28]; 3D incoherent imaging, such as fluorescence imaging [29,30]; and bright-field imaging [31]. Here, by taking the illumination optical-transfer function (OTF) into consideration, we derive a volumetric DPC model to achieve the volumetric phase mapping of thick samples from the snapshot phase-space measurements in partially coherent conditions. Then, we conduct a diffraction tomography process with a phase-point-spread function (PSF) to further improve the resolution together with the optical-sectioning ability across a large DOF, and we finally extract 3D RI information from the volumetric phase map. Experiments on freely moving *Caenorhabditis elegans* are conducted to verify our superior label-free 3D imaging capability for highly dynamic samples.

II. SYSTEM AND METHOD

To verify our method, we build a LFM based on a commercial microscope (Zeiss, Observer Z1), as shown by the schematic diagram in Fig. 1(a). Normal Kohler illumination with a numerical aperture (NA) of 0.55 is applied to form partially coherent illumination. Illumination from a lamp source has a Gaussian-shaped OTF, as shown in Fig. 1(c), rather than the ideally uniform distribution. After passing through the sample and the narrow band-pass fluorescein isothiocyanate filter (MF525-39, Thorlabs), the light is transmitted to the microlens array (MLA) at the image plane by a $4f$ system, which consists of an objective lens (20×/0.5 NA, Zeiss Apochromat) and a tube lens (f =165 mm). The MLA with a 2.1 mm focal length and 100 μm pitch size divides the light field into different spatial-frequency components at different local areas. Then, we use a relay system to conjugate the back focal plane of the MLA to the sensor plane (Andor Zyla 4.2 Plus) for parallel sampling of the phase-space measurements. The magnification of the relay system is set to 0.845, so

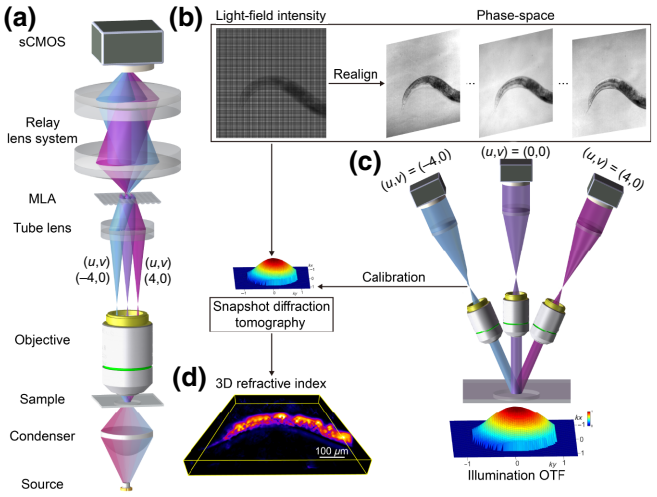

FIG. 1. Schematic of the experimental setup and imaging principle. (a) Experimental setup consists of a conventional microscope with Kohler illumination and light-field detection part. MLA is inserted at the native image plane of the microscope and an scientific complementary metal oxide semiconductor sensor is used to detect the back focal plane of the MLA. Different angular components passing through the sample are marked with different colors. (b) Captured raw data and smoothed phase-space measurements after pixel realignment. (c) Light-field detection can be viewed as wide-field imaging with multiple low-NA objectives from different perspectives under the same illumination OTF. (d) 3D RI distribution is reconstructed using multiple angular measurements under partially coherent illumination with calibrated illumination OTFs.

that each microlens covers around 13 × 13 sensor pixels, which corresponds to the angular resolution.

By phase-space modeling in the LFM [32], the captured image can be realigned into low-resolution smoothed phase-space measurements, as shown in Fig. 1(b). Then, the light-field detection can be viewed as wide-field imaging with multiple low-NA objectives from specific perspectives [Fig. 1(c)]. The phase-space PSFs of the LFM have a much larger DOF than that of wide-field imaging with the same objective NA, providing necessary volumetric information for 3D RI imaging (detailed analysis in Appendix B). Comparatively, traditional QPI methods usually utilize wide-field detection and have an extremely limited DOF, and thus, multiple measurements with axial scanning are often required for observing thick samples.

Our method is inspired by 3D Fourier ptychographic microscopy (FPM) [33], in which the multiple angular components are synthesized to obtain 3D DPC results [6]. However, in the light-emitting diode (LED) array-based FPM system, the angular components are introduced by angular illuminations. Therefore, the illumination NA is much smaller than the detection NA of the objective, resulting in a coherent imaging model. In contrast, the LFM system applies bright-field illumination, where the

illumination NA is much larger than the detection NA of every perspective, and thus, cannot be described in the coherent model. Therefore, we first use the calibrated illumination OTF in a volumetric DPC model to achieve a low-resolution quantitative phase stack from the 4D phase-space measurements. Then a 3D deconvolution using the 3D phase PSF is applied to enhance the resolution and achieve computational optical sectioning.

The basic principle of DPC has been described before [6], in which illumination-based DPC is performed in a LED array microscope. Here, we make some extensions and apply the model to the detection side with a LFM, as shown in Fig. 1(a).

Generally speaking, the quantitative phase gradient is produced by DPC images, which are yielded by normalized subtraction of intensity images from opposite directions. In our proposed method, there are two symmetry axes, producing two directional DPCs, as shown by [34]

$$I_{\mathrm{DPC}_i} = \frac{I_{D_{i,1}} - I_{D_{i,2}}}{I_{D_{i,1}} + I_{D_{i,2}}}, \tag{1}$$

where $i = 1, 2$ and $\{D_{1,1}, D_{1,2}\} = \{\text{left,right}\}$ and $\{D_{2,1}, D_{2,2}\} = \{\text{up,down}\}$ represent the two directions of DPC. These directions represent different angular components in light-field data, corresponding to different illumination angles in traditional DPC. In our setup, we can get four images from a single light-field measurement and each one can be considered as the same wide-field microscope collection with different partially coherent illuminations.

Considering a sample with a complex transmission function, $o(\mathbf{r})$, with $\mathbf{r} = (x, y)$ being the spatial coordinates. The field at the sample plane is the product of the illumination $E(\mathbf{r})$ [Fourier pair $E(\mathbf{u})$] and the sample's transmission function, $o(\mathbf{r})$. Then, the field is convolved with the pupil function, $P(\mathbf{p})$, as a low-pass filter, with $\mathbf{p}$ indicating the spatial frequency coordinates at the pupil plane. The intensity distribution at the capture plane can be expressed as

$$I(\mathbf{r}_c) = |\mathcal{F}^{-1}(P(\mathbf{p})\mathcal{F}\{o(\mathbf{r})\mathcal{F}^{-1}[E(\mathbf{u})]\})|^2, \tag{2}$$

where $\mathbf{r}_c$ denotes the coordinates at the capture plane; $\mathcal{F}(\cdot)$ and $\mathcal{F}^{-1}(\cdot)$ represent the two-dimensional Fourier transform and its inverse transform, respectively.

Although the transfer function between measured intensity and sample's absorption or phase is nonlinear, it can be linearized with the assumption of a weak-scattering object as follows:

$$o(\mathbf{r}) = e^{-\mu(\mathbf{r})+i\varphi(\mathbf{r})} \approx 1 - \mu(\mathbf{r}) + i\varphi(\mathbf{r}), \tag{3}$$

where $\mu(\mathbf{r})$ and $\varphi(\mathbf{r})$ indicate the absorption and phase distribution of the object, respectively. We thus can further simplify Eq. (2) as follows (detailed derivation in Sec. A1 of Appendix A):

$$\widetilde{I}(\mathbf{x}) = \mathbf{B}\delta(\mathbf{x}) + H_{\mathrm{abs}}(\mathbf{x})\tilde{\mu}(\mathbf{x}) + H_{\mathrm{phi}}(\mathbf{x})\tilde{\varphi}(\mathbf{x}), \tag{4}$$

where $\mathbf{B}$ denotes the background term; $H_{\mathrm{abs}}(\mathbf{x})$ and $H_{\mathrm{phi}}(\mathbf{x})$ represent the transfer functions of absorption and phase, respectively.

In Eq. (1), the DPC image is a normalized subtraction of two intensity images from symmetrical angles. Ideally, the DPC image does not contain any absorption information in an aberration-free system, which means $H_{\mathrm{abs}}(x) = 0$. Thus, the DPC image in the Fourier domain and the system transfer function from the phase distribution to DPC image can be expressed as

$$I_{\mathrm{DPC}}(\mathbf{r}) = H_{\mathrm{DPC}}(\mathbf{r}) \cdot \varphi(\mathbf{r}), \tag{5}$$

$$H_{\mathrm{DPC}}(\mathbf{x}) = \frac{H_{\mathrm{phi}}(\mathbf{x})}{\mathbf{B}}, \tag{6}$$

where $\mathbf{B}$ can be approximated as the sum of two images to form the DPC image in Eq. (1).

From the imaging model in Eq. (5), the quantitative phase can be recovered by deconvolution of the DPC image with the estimated transfer function. For the transfer function, the frequencies along the symmetric axis and beyond the frequency range defined by NA are set to zero. When deconvoluting within the frequency range, frequencies with low intensities often lead to amplified noise and artifacts [6]. So, here we apply the Tikhonov regularized deconvolution to solve this optimization problem,

$$\min \sum\nolimits_j \left\| \tilde{I}_{\mathrm{DPC},j} - H_{\mathrm{DPC},j}\tilde{\varphi} \right\|_2^2 + \alpha \left\| \tilde{\varphi} \right\|_2^2, \tag{7}$$

where j is the index of DPC images from different directions (left-right and up-down), and α is a regularization parameter. The quantitative phase at one single plane can then be estimated as

$$\tilde{\varphi} = \mathcal{F}^{-1}\left\{ \frac{\sum_j \tilde{I}_{\mathrm{DPC},j} H^*_{\mathrm{DPC},j}}{\sum_j |H_{\mathrm{DPC},j}|^2 + \alpha} \right\}, \tag{8}$$

After applying this process to the phase-space stack at different axial planes generated by a single light-field measurement [35], we can obtain a wide-field phase stack. To further enhance the resolution and remove the out-of-focus components, we then apply 3D phase deconvolution with a simulated 3D phase PSF, which is similar to the phase-space deconvolution process in fluorescence imaging [36] (detailed derivation in Sec. A2 of Appendix A). Then, the reconstructed volumetric phase map is transformed into the RI distribution by $\Delta n = (\lambda\varphi)/(2\pi d)$, where d represents the depth of one slice in the sample.

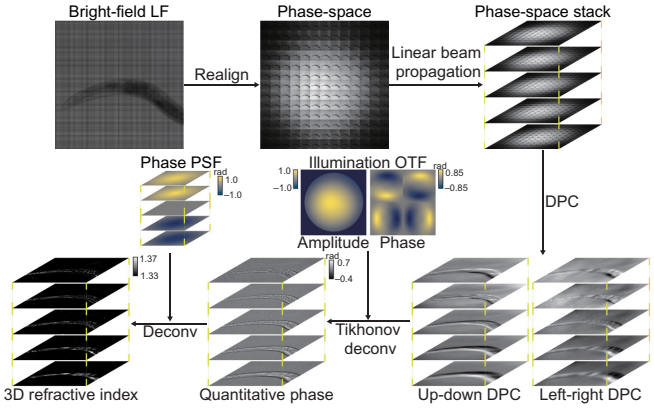

FIG. 2. Pipeline of snapshot partially coherent diffraction tomography. First, the light-field (LF) image captured with partially coherent illumination is realigned as phase-space measurements. Next, we apply digital linear-beam propagation to estimate phase-space measurements at different axial planes, which are used for directional 3D DPC images. Then, calibrated illumination OTF is used with Tikhonov deconvolution to obtain a quantitative phase stack. Finally, we apply 3D RL deconvolution with a simulated phase PSF for enhanced resolution and optical sectioning and use a linear transform to acquire 3D RI distribution.

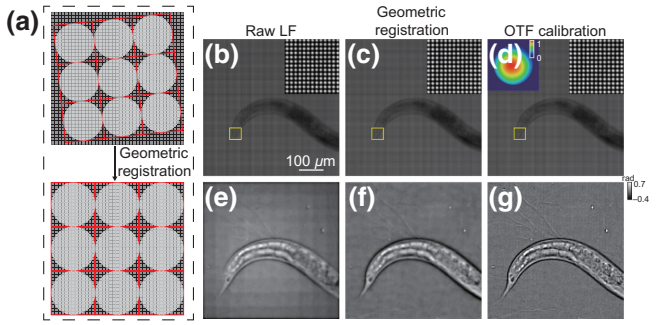

FIG. 3. Performance of geometric registration and OTF calibration. (a) Illustration of geometric registrations to correct misalignment between MLA and sensor, including subpixel shift, tilting, and magnification mismatch. (b) Raw light-field image. (c) Light-field image after geometric registration. (d) Light-field image with the calibrated OTF amplitude shown in the inset. Reconstructed quantitative phase at native objective plane without calibration (e), with geometric registration (f), and with both geometric registration and OTF calibration (g). Scale bars, 100 μm.

Specifically, our algorithm can be described by the following steps, as shown in Fig. 2. First, the captured light-field image is realigned into 13×13 angular components. The pixels corresponding to a certain angular component of each microlens can be recombined into a subimage under a specific subaperture. Then, linear-beam propagation can be applied to produce the phase-space measurements at different axial planes [37]. Next, we calculate the left-right and up-down directional DPC stacks [6] from the phase-space stack, as described by Eq. (1). With the calibrated illumination OTF, the quantitative phase stack can then be retrieved by solving the Tikhonov-regularized optimization problem, as described in Eq. (7). Finally, we apply a 3D RL deconvolution with the phase PSF to decouple the 3D phase information within the extended DOF for computational optical sectioning and spatial-resolution enhancement. The detailed process is given by Eqs (A14) and (A15). The phase PSF used here is generated by imaging a subdiffraction-limit phase point at different axial planes during the numerical simulation.

III. RESULTS

It is inevitable that there are some distortions in the experimental system, such as shift, tilting, and magnification mismatch, which lead to inaccurate phase estimation during DPC calculations. To solve this problem, we apply both the geometric registration of raw light-field measurements and the calibration of illumination OTF on experimental data. We demonstrate the effectiveness of the abovementioned system calibration by imaging a fixed *C. elegans*, which is put on a Petri dish and embedded in 2% agarose gel. Without geometric registration, the recovered phase has a bulging background and some rectangular artifacts, as shown in Figs. 3(b) and 3(e). These system errors are mainly caused by the tilting and magnification mismatch between the MLA and the sensor, as shown in Fig. 3(a). The image registration of alignment errors is performed using the coefficients estimated from measuring a uniform plane without a sample. Besides the alignment errors in the LFM, the nonuniform distribution of the light source will lead to an inaccurate estimation of the quantitative phase, akin to lower weights on high-frequency components than low-frequency components. Then, the spatial resolution will be significantly decreased, as shown in Fig. 3(f). To obtain an accurate estimation of the amplitude of the illumination OTF, we image a uniform plane as a reference. The sum of different angular images can be used as an experimental OTF amplitude. With the calibrated OTF [Fig. 3(d)], much more detailed structures of the sample can be observed from the retrieved phase information, as shown in Fig. 3(g).

To evaluate the quantification accuracy and resolution of our method, we measure the quantitative phase target (QPT, Benchmark Technologies Corporation) for analysis. Figure 4(a)–4(c) show the bright-field images of the QPT USAF targets with different feature heights (150, 200, and 350 μm, respectively) under partially coherent illumination. Since the phase target only contains obvious phase differences, the captured images have low intensity contrast, as the red line profiles show in Figs. 4(a)–4(c). The phase maps recovered by our method for the same QPT USAF targets as those in Figs. 4(a)–4(c) are shown in Figs.

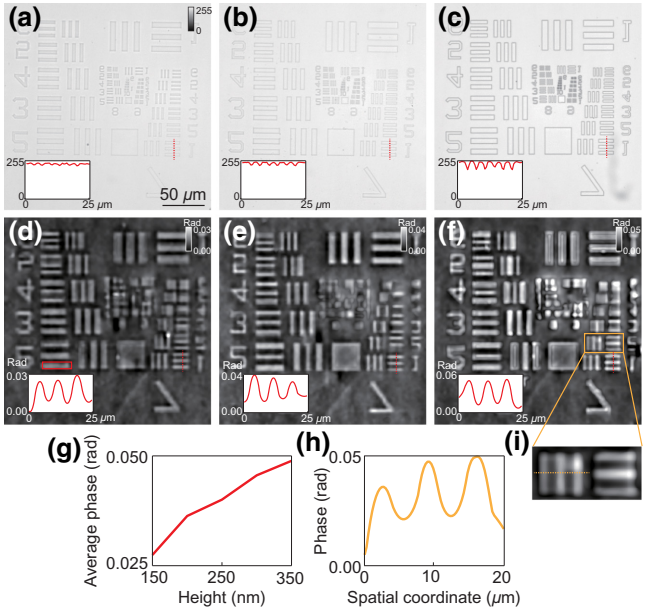

FIG. 4. Experimental and quantitative analysis of the QPT USAF target part. Bright-field image of the QPT USAF target part with different feature heights under partially coherent illumination; the feature heights are (a) 150 nm, (b) 200 nm, and (c) 350 nm. (d)–(f) Recovered phase map of the same targets in (a)–(c). Line profiles of the red dashed line of each image are shown in the bottom-left corner. (g) Average phase of the specified region of the USAF targets with different feature heights from 150 to 350 nm. Selected region is marked as the red box in (d). (h) Profile of the yellow dashed line in (i). (i) Enlarged view of the yellow boxed region in (f). Scale bar, 50 μm.

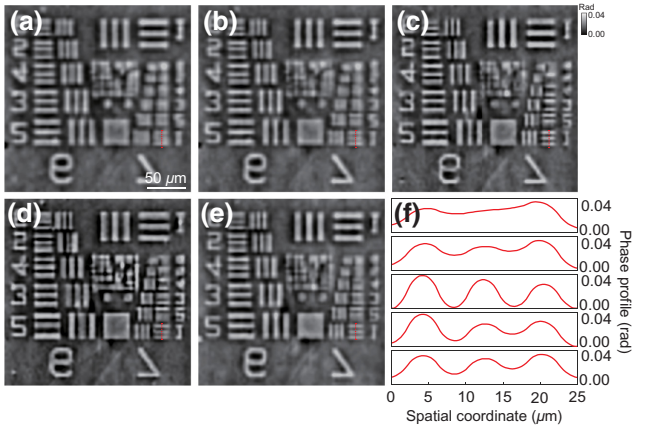

FIG. 5. Experimental analysis of the depth of field using QPT USAF target part. Recovered phase map of the QPT USAF target part of same feature height (200 nm) focused at different axial positions of (a) −12.0 μm, (b) −9.0 μm, (c) 0 μm, (d) 6.0 μm, and (e) 12.0 μm. (f) Line profiles of red dashed lines in (a)–(e). These line profiles correspond to (a)–(e) from top to bottom. Scale bar, 50 μm.

4(d)–4(e), in which the line profiles of group 7, element 1, are shown with high contrast to the background. Different bars of the same elements inside a certain USAF target have similar phase values, indicating that they have the same physical heights. To better evaluate the accuracy of our method quantitatively, we select the specified region of the USAF targets [red box in Fig. 4(d)] for comparison. After averaging the values in each region, we find that the averaged phases of the targets with different feature heights have an obvious linear relationship with their real physical heights, as shown in Fig. 4(g). From the results, we can see that our method can obtain quantitative phase imaging with a resolution of 3.48 μm (group 7, element 2) by using the objective lens with 0.5 NA in the LF microscope.

The DOF has always been one of the most concerning issues of quantitative-phase-imaging techniques, so we analyze the DOF of our method on the QPT USAF target part with a feature height of 200 nm. We roughly focus on the surface of the target part and consider it as the $z = 0$ plane. Then several images focused at different axial positions from −12.0 to 12.0 μm are captured to demonstrate the relative extended DOF of the proposed method, as shown in Figs. 5(a)–5(e). The focused axial positions in Figs. 5(a)–5(e) are −12.0, −9.0, 0, 6.0, and 12.0 μm, respectively. For clear characterization, the line profiles of the red dashed lines in Figs. 5(a)–5(e) are shown in Fig. 5(f) to reveal the axial range of clear imaging based on group 7, element 1, of the QPT USAF targets. It is not possible to resolve these three bars of the target part focused at −12.0 μm, but they can be resolved from −9.0 to 12 μm. The resolving ability of our method reaches its peak at around 0 μm and the line profile has lower contrast when the defocus becomes larger. Here, we can simply summarize that the DOF of our method is over 21.0 μm when we maintain a resolution better than 3.48 μm (group 7, element 2).

We show the successive reconstruction processes of a 3D RI distribution from a single light-field image in Fig. 6. By applying the digital linear-beam propagation, we can estimate the 4D phase-space measurements over a wide range of axial depths from −45 to 45 μm with a step of 1.5 μm. Then, the quantitative directional DPC images at corresponding axial planes can be obtained, illustrating the phase gradient in different directions, as shown in the first two rows of Fig. 6(a). With the precalibrated illumination OTF, we can recover the quantitative phase stack based on Eq. (7) with the Tikhonov regularization deconvolution. The quantitative phase images show more detailed structures, but some background remains, which comes from the out-of-focus information of the extended DOF. After 3D RL deconvolution with the simulated phase PSF with the same objective NA, we can extract the 3D RI distribution from the deconvolved phase stack with both enhanced resolution and optical-sectioning ability. The slices at different axial planes are shown in the last row of Fig. 6(a).

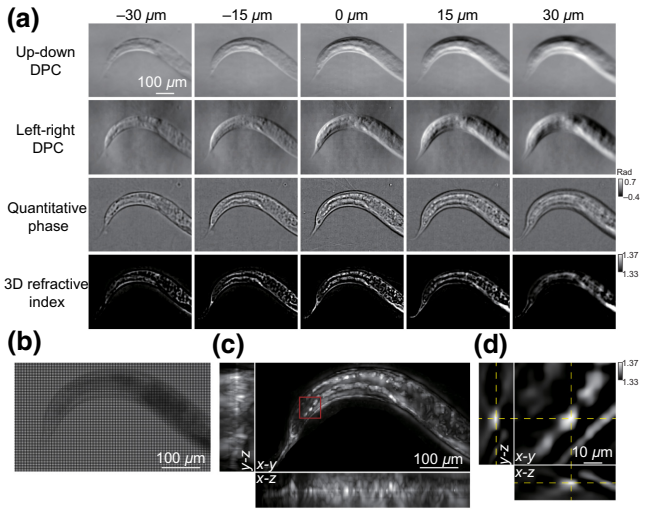

FIG. 6. Successive reconstruction processes of fixed *C. elegans*. (a) First row, up-down DPC images. Second row, left-right DPC images. Third row, quantitative phase stack. Fourth row, reconstructed RI distribution. Different columns correspond to different axial positions. All results are generated from a single light-field image (b). Scale bars, 100 μm. (c) Orthogonal maximum-intensity projections (MIPs) of the 3D RI distribution. Scale bars, 100 μm. (d) Orthogonal slices of the magnified view marked with a red box in (c) along the marked yellow dashed line. Scale bars, 10 μm.

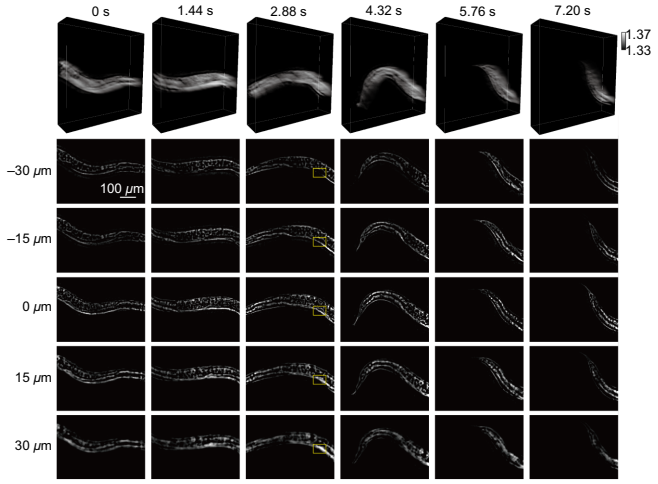

FIG. 7. 3D RI tomography of freely moving *C. elegans*. 3D RI distribution of freely moving *C. elegans* at different time stamps marked on the top. Video is captured at 30 Hz (Video 1 within the Supplemental Material [40]). Projections from a specific perspective are shown in the first row. Multiple slices at different axial positions labeled on the left are shown below. Scale bars, 100 μm.

Similar to traditional 3D fluorescence imaging by LFM [32], the reconstructed 3D RI imaging using our method has the highest spatial resolution at the axial position close to the native objective plane. The achievable resolution will gradually decrease with an increase of the defocus distance due to the inaccurate approximation of linear-beam propagation. A better beam-propagation model and other hardware modifications [38] can be exploited in the future to further improve the spatial resolution. The orthogonal MIPs of the recovered RI distribution are also shown in Fig. 6(c). Orthogonal slices of a magnified view of the area marked by the red box in Fig. 6(c) are visualized in Fig. 6(d) to show the optical-sectioning capability. Considering the large size of the reconstructed volume, containing around 300 megavoxels ($2048 \times 2048 \times 61$ voxels), the whole procedure takes about 30 min on a computer with an i7-7800X CPU and one TITAN-Xp GPU. Optimization of reconstruction algorithms can be exploited in the future to accelerate the reconstruction process and enable video-rate visualization.

To further demonstrate the snapshot label-free 3D imaging capability of our method, we image a freely moving *C. elegans* in Fig. 7 and Video 1 within the Supplemental Material [40]. Different from the experiments above, we select several energetic *C. elegans* and image them on a glass-bottomed dish. Traditional DPC-based RI recovery methods [6,17] often require multiple acquisitions to achieve differential intensities, which make them extremely difficult to use for observing living organisms. Accordingly, the samples imaged by previous methods are usually fixed or anesthetized, since the motion of the sample will introduce strong artifacts in reconstructions with multiple frames. On the contrary, our method captures the whole 3D RI distribution within a snapshot across a large DOF. We record the whole process of the *C. elegans* moving out from the current field of view at 30 Hz for 11 s. As shown in Fig. 7, we select several specific moments with typical postures to show the fast dynamics observed of the living organisms. In the first row, the MIPs from a particular perspective show the moving track and body posture, which can be utilized for activity and behavior analysis. In other rows, the slices at different axial planes are shown to demonstrate the consistency in both the axial domain and temporal dimension with good optical-sectioning capability. For example, at a time of 2.88 s, it is obvious that a vesicle in the yellow box is gradually shaped as the axial position drifts away. From 4.32 to 7.20 s, the relative RI distribution at the tail region remains almost the same. In this experiment, we capture the crawling of *C. elegans*. Besides, our method can also be extended to observe other behaviors of *C. elegans*, such as seizures and mating. The high spatial-temporal resolution of our method is necessary for various practical applications, such as clinical inspections and dynamic wavefront estimations in adaptive optics [1].

IV. CONCLUSION

We demonstrate a snapshot partially coherent diffraction tomography method based on LFM with a volumetric DPC model in deep tissue. We validate our proposed method by imaging freely moving *C. elegans* at 30 Hz across a large volume. Apart from that, the proposed method can be easily implemented on an existing light microscope with simple hardware modifications and without the requirement for a laser source. With the increasing demand for dynamic 3D RI imaging in complicated environments, our method can work as a robust and low-cost add-on, which is generally accessible for broad communities, including both optics and biology.

ACKNOWLEDGMENTS

We thank Guangshuo Ou for providing the *C. elegans*. The authors gratefully acknowledge support from the Beijing Municipal Science & Technology Commission (BMSTC) (Grant No. Z181100003118014), the National Key Research and Development Program of China (Grant No. 2020AAA0130000), and the Tsinghua University Initiative Scientific Research Program. J.W. sincerely appreciates funding from the Postdoctoral Science Foundation of China (Grant No. 2019M660644) and the National Postdoctoral Program for Innovative Talent. Y.Z. is supported by the Natural Science Foundation of Jiangsu Province (Grant No. BK20190292).

APPENDIX A: DETAILED DERIVATION FOR THEORETICAL MODEL

1. Detailed derivation of partially coherent quantitative DPC in LFM

In our experimental setup shown in Fig. 1, we have the same illumination source with different detection angles of corresponding subapertures. Such an imaging scheme is very similar to imaging the sample in the same direction with different angular illumination sources. For an $N \times N$ (pixel numbers after each microlens) light field, the angular domain (u, v) is divided into $N \times N$ components. The left part refers to those components of $[(u, v)|u < (N/2)]$. When we rewrite a light-field image into a four-dimensional matrix, $L(x, y, u, v)$, we can obtain

$$I_{\text{left}}(x, y) = \sum_{u=1}^{(N-1)/2} \sum_{v=1}^{N} L(x, y, u, v), \tag{A1}$$

$$I_{\text{right}}(x, y) = \sum_{u=(N+1)/2}^{N} \sum_{v=1}^{N} L(x, y, u, v), \tag{A2}$$

From Eqs. (A1) and (A2), we can get four images from a single frame of light-field measurement, which can be considered as the same wide-field microscope collection with different partially coherent illumination and described by the same imaging model as Eq. (2).

In detail, Eq. (2) can be reorganized as

$$I(\mathbf{r}_c) = \left| \iint \iint \iint E(\mathbf{u}) o(\mathbf{r}) P(\mathbf{p}) e^{-i2\pi(\mathbf{u}\cdot\mathbf{r})} e^{i2\pi(\mathbf{r}\cdot\mathbf{p})} \times e^{i2\pi(\mathbf{p}\cdot\mathbf{r}_c)} d^2\mathbf{u} d^2\mathbf{r} d^2\mathbf{p} \right|^2, \tag{A3}$$

For partially coherent illumination at the sample, with $E(\mathbf{u})E^*(\mathbf{v}) = |E(\mathbf{u})|^2 \delta(\mathbf{u} - \mathbf{v})$ and the illumination power $S(\mathbf{u}) = |E(\mathbf{u})|^2$ corresponding to the angular intensity distribution of illumination, the captured intensity is the incoherent sum of images formed by each coherent source with a single incident angle. Equation (A3) can be expressed as

$$I(\mathbf{r}_c) = \iint S(\mathbf{u}) \left| \iint P(\mathbf{p}) \left[\iint o(\mathbf{r}) e^{i2\pi(\mathbf{p}-\mathbf{u})\cdot\mathbf{r}} d^2\mathbf{r} \right] \times e^{i2\pi(\mathbf{p}\cdot\mathbf{r}_c)} d^2\mathbf{p} \right| d^2\mathbf{u}, \tag{A4}$$

Substituting $\mathbf{m} = \mathbf{p} - \mathbf{u}$ and $O(\mathbf{m}) = \mathcal{F}[o(\mathbf{r})]$ and using the identity $\left|\int f(\mathbf{m}) d\mathbf{m}\right|^2 = \iint f(\mathbf{m}) f^*(\mathbf{n}) d\mathbf{m} d\mathbf{n}$, we can obtain, with the consideration that the pupil function $P(\mathbf{p})$ is an even function, the following:

$$I(\mathbf{r}_c) = \iint \iint O(\mathbf{m}) O^*(\mathbf{n}) \left[\iint S(\mathbf{u}) P(\mathbf{m} + \mathbf{u}) \times P^*(\mathbf{n} + \mathbf{u}) d^2\mathbf{u} \right] e^{i2\pi[\mathbf{r}_c(\mathbf{m}-\mathbf{n})]} d^2\mathbf{m} d^2\mathbf{n}, \tag{A5}$$

where $\mathbf{m}$ and $\mathbf{n}$ are variables for integration in the spatial frequency space. We use H to represent the system transfer function $H(\mathbf{m}, \mathbf{n}) = \iint S(\mathbf{u}) P(\mathbf{m} + \mathbf{u}) P^*(\mathbf{n} + \mathbf{u}) d^2\mathbf{u}$,

$$I(\mathbf{r}_c) = \iint \iint O(\mathbf{m}) O^*(\mathbf{n}) H(\mathbf{m}, \mathbf{n}) e^{i2\pi[\mathbf{r}_c(\mathbf{m}-\mathbf{n})]} d^2\mathbf{m} d^2\mathbf{n}, \tag{A6}$$

Substituting $\mathbf{x} = \mathbf{m} - \mathbf{n}$ and rewriting Eq. (A6) in the Fourier space of the captured plane $\mathbf{x}$, we can get

$$\widetilde{I}(\mathbf{x}) = \iint O(\mathbf{m}) O^*(\mathbf{m} - \mathbf{x}) H(\mathbf{m}, \mathbf{m} - \mathbf{x}) d^2\mathbf{m}, \tag{A7}$$

Equation (A7) denotes the four-dimensional transfer function for the partially coherent illumination [39], which is performed as a four-dimensional convolution with complex conjugate terms.

Considering the weak-scattering assumption in Eq. (3), the Fourier transform of $o(\mathbf{r})$ is

$$O(\mathbf{m}) = \delta(\mathbf{m}) - M(\mathbf{m}) + i\Phi(\mathbf{m}), \tag{A8}$$

where $M(\mathbf{m})$ and $\Phi(\mathbf{m})$ are the Fourier transforms of $\mu(\mathbf{r})$ and $\varphi(\mathbf{r})$, respectively. Neglecting the small cross term between M and Φ, the product of the Fourier-transformed object function in Eq. (A7) can be rewritten as

$$\begin{aligned} O(\mathbf{m})O^*(\mathbf{n}) \approx{}& \delta(\mathbf{m})\delta(\mathbf{n}) - [M(\mathbf{m})\delta(\mathbf{n}) + M^*(\mathbf{n})\delta(\mathbf{m})] \\ &+ i[\Phi(\mathbf{m})\delta(\mathbf{n}) - \Phi^*(\mathbf{n})\delta(\mathbf{m})], \end{aligned} \tag{A9}$$

Substituting Eq. (A9) into Eq. (A7), we can get Eq. (4), where $\mathbf{B}$ denotes the background term and $H_{\text{abs}}(\mathbf{x})$ and $H_{\text{phi}}(\mathbf{x})$ represent transfer functions of absorption and phase, respectively. In detail, letting $\mathbf{x}'$ denote the integration variable,

$$\mathbf{B} = \iint S(\mathbf{x}')P(\mathbf{x}')P^*(\mathbf{x}')d^2\mathbf{x}', \tag{A10}$$

$$\begin{aligned} H_{\text{abs}}(\mathbf{x}) = -\Bigg[&\iint S(\mathbf{x}')P(\mathbf{x}'+\mathbf{x})P^*(\mathbf{x}')d^2\mathbf{x}' \\ &+ \iint S(\mathbf{x}')P(\mathbf{x}'-\mathbf{x})P^*(\mathbf{x}')d^2\mathbf{x}'\Bigg], \end{aligned} \tag{A11}$$

$$\begin{aligned} H_{\text{phi}}(\mathbf{x}) = i\Bigg[&\iint S(\mathbf{x}')P(\mathbf{x}'+\mathbf{x})P^*(\mathbf{x}')d^2\mathbf{x}' \\ &- \iint S(\mathbf{x}')P(\mathbf{x}'-\mathbf{x})P^*(\mathbf{x}')d^2\mathbf{x}'\Bigg], \end{aligned} \tag{A12}$$

Ideally, since $H_{\text{abs}}(x) = 0$, we can get Eqs (5) and (6) from Eq. (4). In detail, Eq. (6) can be expressed as

$$\begin{aligned} H_{\text{DPC}}(\mathbf{x}) &= \frac{H_{\text{phi}}(\mathbf{x})}{\mathbf{B}} \\ &= \frac{i\iint S(\mathbf{x}')[P(\mathbf{x}'+\mathbf{x}) - P(\mathbf{x}'-\mathbf{x})]P^*(\mathbf{x}')d^2\mathbf{x}'}{\iint S(\mathbf{x}')P(\mathbf{x}')P^*(\mathbf{x}')d^2\mathbf{x}'}, \end{aligned} \tag{A13}$$

After applying the Tikhonov-regularized deconvolution to the optimization problem in Eq. (7), we obtain an estimation of the quantitative phase at one single plane as Eq. (8).

2. 3D phase deconvolution formation

Since the DPC images in Eq. (1) are calculated by using all angular components covering the whole aperture, the phase PSF is generated by imaging a subdiffraction-limit point with full NA of the objective in numerical simulation. We assume that each layer of the recovered preliminary volumetric phase is the weighted integral of the whole volume along the 3D phase PSF, which is spatially invariant. To solve this deconvolution problem, we apply Richardson-Lucy (R-L) deconvolution to every recovered phase image at different axial depths with corresponding 3D phase PSF, and then calculate the weighted average of these volumes after deconvolution, which is taken as the initial value of the next iteration. Specifically, the iteration process of R-L deconvolution to each phase image at different axial position is similar to the deconvolution to each image from different acquisition angles [32], in which the update of the 3D phase map is done slice by slice, according to the Eqs (A14) and (A15),

$$X_i^{(k+1)} \leftarrow X_i^{(k)} \odot \{\widetilde{Y}_i./[G_i X^{(k)}]G_i\}./(\mathbf{1}^T G_i), \tag{A14}$$

$$X^{(k+1)} = \frac{1}{N}\sum\nolimits_i X_i^{(k+1)}, \tag{A15}$$

where $\odot$ represents the dot product operator, $./$ represents the point division operator, and $\widetilde{Y}_i$ is the estimated quantitative phase at the ith axial plane. $X_i^{(k)}$ is the deconvolved volume of $\widetilde{Y}_i$ after k iterations, G_i is the phase PSF of the corresponding axial plane i, and N is the total number of axial planes.

APPENDIX B: EXTENDED DEPTH OF FIELD

QPI based on partially coherent illumination has a coherence length that is proportional to the system depth of the field. We can only calculate the phase result of the sample that is located in the system depth of the field. Since our algorithm calculates the phase from the intensity difference, the resolution of the intensity images will affect the phase resolution. Theoretically, LFM captures the 4D phase-space information within a snapshot, but there is a trade-off between spatial and angular resolution. More specifically, LFM divides the whole aperture into several subapertures (13×13 here), which extends the depth of field but sacrifices spatial resolution for each subapertures due to the low sampling density in the spatial domain. Figure 8(a) shows the PSF of an unfocused LFM with orthogonal slices, while Fig. 8(b) shows the PSF of wide-field microscopy (WFM) for comparison. Different from WFM, LFM can keep the photons focused within a much larger depth of field. As shown in Fig. 8(d), the WFM PSF has a smaller FWHM at the focal plane, corresponding to higher spatial resolution at the native objective plane, while its FWHM expands much faster along the Z axis. Conversely, the FWHM of the LFM PSF remains similar across a large depth range, suggesting the capability for phase imaging of a large volume. To make a detailed description, we choose two angular components [$(u, v) = (0, 0)$, $(u, v) = (-5, 0)$] from the LFM PSF after pixel realignment into the phase space, as shown in Fig. 8(c). Compared with wide-field PSF, the multiangular PSFs with different subapertures have almost constant intensity and FWHM over a relatively large range of the Z axis.

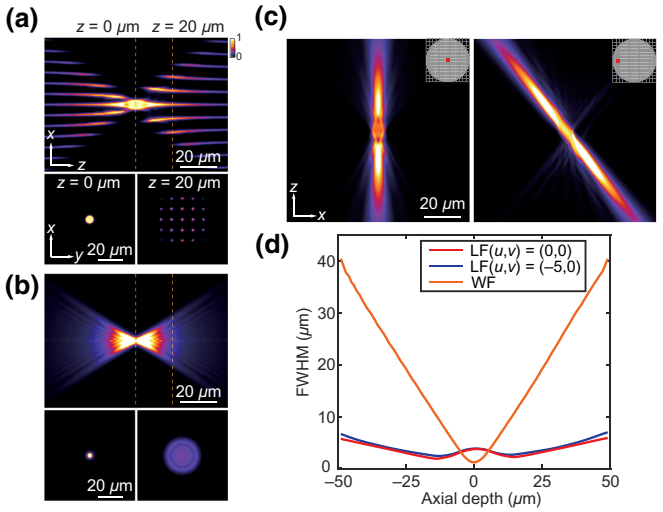

FIG. 8. Quantitative comparison between light-field PSF and wide-field PSF. (a) Orthogonal slices of simulated light-field PSF at y=0 μm and z=0 μm, 20 μm planes. (b) Orthogonal slices of simulated wide-field PSF at corresponding planes for comparison. (c) X-Z slices at y=0 μm plane of different angular components $[(u, v) = (0, 0), (u, v) = (-5, 0)]$ of simulated light-field PSF after pixel realignment. (d) FWHM curves of different angular components of simulated light-field PSF and simulated wide-field PSF, illustrating that light-field PSFs have a much larger depth of field than the wide-field PSF. Scale bar, 20 μm.

Although the lateral resolution of LFM is reduced due to insufficient sampling in the spatial domain, the resolution of phase imaging may be enhanced by the tomographic process with a high accuracy of phase measurements, which can be an interesting topic to be exploited in the future.

APPENDIX C: COMPARISON BETWEEN RECONSTRUCTIONS USING DIFFERENT PSFS

To compare the imaging performance of the experimental PSF with the simulated PSF, we experimentally measure the system PSF as follows. We dilute the 2-μm-polymer-bead solution (Thermo Fisher Scientific, F-8888, 2 μm) to 1:2500, then select one appropriate region to take phase-space measurements at different axial planes. Then, we calculate the DPC stacks and perform the deconvolution to get an experimental 3D phase PSF stack. The results using the simulated PSF and the experimental PSF are shown in Fig. 9, which shows the reconstructed RI distribution from −30 to 30 μm. Although the reconstructed RI map at 30 μm with the experimental PSF shows better resolution than that using the simulated PSF, the RI maps at other layers with the experimental PSF retain fewer details, compared with the result of the simulated PSF. Because their performances are similar, we keep using

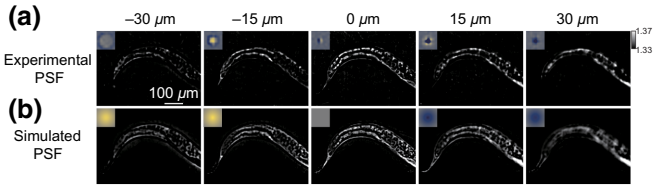

FIG. 9. Comparison between the 3D RI map reconstructed with the experimental PSF and that using the simulated PSF. (a) Reconstructed RI distribution by using experimental-phase PSF for deconvolution. (b) Reconstructed RI distribution by using simulated-phase PSF for deconvolution. Scale bars, 100 μm.

the simulated PSF to reconstruct the 3D RI map in all experiments.

[1] Y. Park, C. Depeursinge, and G. Popescu, Quantitative phase imaging in biomedicine, Nat. Photonics **12**, 578 (2018).

[2] W. Choi, C. Fang-Yen, K. Badizadegan, S. Oh, N. Lue, R. R. Dasari, and M. S. Feld, Tomographic phase microscopy, Nat. Methods **4**, 717 (2007).

[3] K. J. Stout and L. Blunt, *Three Dimensional Surface Topography* (Elsevier, London, England, 2000).

[4] G. Nomarski, in *Journal de Physique et le Radium*. (EDP SCIENCES, Les Ulis Cedexa, France, 1955), Vol. 16, pp. S88-S88.

[5] F. Zernike, How I discovered phase contrast, Science **121**, 345 (1955).

[6] L. Tian and L. Waller, Quantitative differential phase contrast imaging in an LED array microscope, Opt. Express **23**, 11394 (2015).

[7] G. Popescu, *Quantitative Phase Imaging of Cells and Tissues* (McGraw Hill Professional, New York, 2011).

[8] Z. El-Schich, A. Leida Mölder, and A. Gjörloff Wingren, Quantitative phase imaging for label-free analysis of cancer cells—focus on digital holographic microscopy, Appl. Sci. **8**, 1027 (2018).

[9] K. Kim, Z. Yaqoob, K. Lee, J. W. Kang, Y. Choi, P. Hosseini, P. T. So, and Y. Park, Diffraction optical tomography using a quantitative phase imaging unit, Opt. Lett. **39**, 6935 (2014).

[10] K. Kim, K. S. Kim, H. Park, J. C. Ye, and Y. Park, Real-time visualization of 3-D dynamic microscopic objects using optical diffraction tomography, Opt. Express **21**, 32269 (2013).

[11] P. Samsheerali, K. Khare, and J. Joseph, Quantitative phase imaging with single shot digital holography, Opt. Commun. **319**, 85 (2014).

[12] P. A. Sandoz, C. Tremblay, S. Equis, S. Pop, L. Pollaro, Y. Cotte, G. F. Van Der Goot, and M. Frechin, Label free 3D analysis of organelles in living cells by refractive index shows pre-mitotic organelle spinning in mammalian stem cells, BioRxiv, 407239 (2018).

[13] G. Kim, M. Lee, S. Youn, E. Lee, D. Kwon, J. Shin, S. Lee, Y. S. Lee, and Y. Park, Measurements of three-dimensional refractive index tomography and membrane deformability

of live erythrocytes from pelophylax nigromaculatus, Sci. Rep. **8**, 9192 (2018).
[14] L. Tian, J. Wang, and L. Waller, 3D differential phase-contrast microscopy with computational illumination using an LED array, Opt. Lett. **39**, 1326 (2014).
[15] C. Zuo, J. Sun, J. Li, J. Zhang, A. Asundi, and Q. Chen, High-resolution transport-of-intensity quantitative phase microscopy with annular illumination, Sci. Rep. **7**, 7654 (2017).
[16] R. Ling, W. Tahir, H.-Y. Lin, H. Lee, and L. Tian, High-throughput intensity diffraction tomography with a computational microscope, Biomed. Opt. Express **9**, 2130 (2018).
[17] P. Ledwig and F. E. Robles, Epi-mode tomographic quantitative phase imaging in thick scattering samples, Biomed. Opt. Express **10**, 3605 (2019).
[18] C. Zuo, Q. Chen, W. Qu, and A. Asundi, Noninterferometric single-shot quantitative phase microscopy, Opt. Lett. **38**, 3538 (2013).
[19] J. Wu, X. Lin, Y. Liu, J. Suo, and Q. Dai, Coded aperture pair for quantitative phase imaging, Opt. Lett. **39**, 5776 (2014).
[20] S. R. P. Pavani, A. R. Libertun, S. V. King, and C. J. Cogswell, Quantitative structured-illumination phase microscopy, Appl. Opt. **47**, 15 (2008).
[21] M. Zhang, J. Wu, J. Suo, H. Xie, J. Fan, and Q. Dai, Snapshot quantitative phase microscopy with a printed film, Opt. Express **26**, 24763 (2018).
[22] J. Li, Q. Chen, J. Sun, J. Zhang, J. Ding, and C. Zuo, Three-dimensional tomographic microscopy technique with multi-frequency combination with partially coherent illuminations, Biomed. Opt. Express **9**, 2526 (2018).
[23] J. M. Soto, J. A. Rodrigo, and T. Alieva, Label-free quantitative 3D tomographic imaging for partially coherent light microscopy, Opt. Express **25**, 15699 (2017).
[24] J. Li, A. Matlock, Y. Li, Q. Chen, C. Zuo, and L. Tian, High-speed in vitro intensity diffraction tomography, Adv. Photon. **1**, 066004 (2019).
[25] S. Chowdhury, M. Chen, R. Eckert, D. Ren, F. Wu, N. Repina, and L. Waller, High-resolution 3D refractive index microscopy of multiple-scattering samples from intensity images, Optica **6**, 1211 (2019).
[26] A. Matlock and L. Tian, High-throughput, volumetric quantitative phase imaging with multiplexed intensity diffraction tomography, Biomed. Opt. Express **10**, 6432 (2019).
[27] K. Lee, K. Kim, G. Kim, S. Shin, and Y. Park, Time-multiplexed structured illumination using a DMD for optical diffraction tomography, Opt. Lett. **42**, 999 (2017).
[28] Z. Zhang, Z. Chen, S. Rehman, and G. Barbastathis, Phase imaging using shifted wavefront sensor images, Opt. Lett. **39**, 6177 (2014).
[29] M. Broxton, L. Grosenick, S. Yang, N. Cohen, A. Andalman, K. Deisseroth, and M. Levoy, Wave optics theory and 3-D deconvolution for the light field microscope, Opt. Express **21**, 25418 (2013).
[30] Y. Sung, Snapshot Projection Optical Tomography, Phys. Rev. Appl. **13**, 054048 (2020).
[31] M. Levoy, R. Ng, A. Adams, M. Footer, and M. Horowitz, in *ACM SIGGRAPH 2006 Papers* (Association for Computing Machinery, New York, NY, USA, 2006), pp. 924.
[32] Z. Lu, J. Wu, H. Qiao, Y. Zhou, T. Yan, Z. Zhou, X. Zhang, J. Fan, and Q. Dai, Phase-space deconvolution for light field microscopy, Opt. Express **27**, 18131 (2019).
[33] R. Horstmeyer, J. Chung, X. Ou, G. Zheng, and C. Yang, Diffraction tomography with Fourier ptychography, Optica **3**, 827 (2016).
[34] M. H. Maleki and A. J. Devaney, Phase-retrieval and intensity-only reconstruction algorithms for optical diffraction tomography, J. Opt. Soc. Am. A **10**, 1086 (1993).
[35] B. Wilburn, N. Joshi, V. Vaish, E.-V. Talvala, E. Antunez, A. Barth, A. Adams, M. Horowitz, and M. Levoy, in *ACM Trans. Graph.* (Association for Computing Machinery, New York, NY, USA, 2005), pp. 765.
[36] P. Sarder and A. Nehorai, Deconvolution methods for 3-D fluorescence microscopy images, IEEE Signal Process. Mag. **23**, 32 (2006).
[37] L. Waller, G. Situ, and J. W. Fleischer, Phase-space measurement and coherence synthesis of optical beams, Nat. Photonics **6**, 474 (2012).
[38] J. Wu, Z. Lu, H. Qiao, X. Zhang, K. Zhanghao, H. Xie, T. Yan, G. Zhang, X. Li, Z. Jiang, X. Lin, L. Fang, B. Zhou, J. Fan, P. Xi, and Q. Dai, 3D observation of large-scale subcellular dynamics in vivo at the millisecond scale, BioRxiv, 672584 (2019).
[39] M. Born and E. Wolf, *Principles of Optics: Electromagnetic Theory of Propagation, Interference and Diffraction of Light* (Elsevier, Oxford, New York, 2013).
[40] See the Supplemental Material at http://link.aps.org/supplemental/10.1103/PhysRevApplied.15.044048 for a time-lapse 3D phase reconstruction of freely moving *C. elegans*.